remote sensing

MDPI

Article

Calibration of Dual-Polarised Antennas for Air-Coupled Ground Penetrating Radar Applications

Samuel J. I. Forster *, Anthony J. Peyton and Frank J. W. Podd

Department of Electrical and Electronic Engineering, The University of Manchester, Oxford Rd, Manchester M13 9PL, UK; a.peyton@manchester.ac.uk (A.J.P.); frank.podd@manchester.ac.uk (F.J.W.P.)
* Correspondence: samuel.forster@postgrad.manchester.ac.uk

Abstract: Radar polarimetry is a technique that can be used to enhance target detection, identification and classification; however, the quality of these measurements can be significantly influenced by the characteristics of the radar antenna. For an accurate and reliable system, the calibration of the antenna is vitally important to mitigate these effects. This study presents a methodology to calibrate Ultra-Wideband (UWB) dual-polarised antennas in the near-field using a thin elongated metallic cylinder as the calibration object. The calibration process involves measuring the scattering matrix of the metallic cylinder as it is rotated, in this case producing 100 distinct scattering matrices from which the calibration parameters are derived, facilitating a robust and stable solution. The calibration procedure was tested and validated using a Vector Network Analyser (VNA) and two quad-ridged antennas, which presented different performance levels. The calibration methodology demonstrated notable improvements, aligning the performance of both functioning and under-performing antennas to equivalent specifications. Mid-band validation measurements indicated minimal co-polar channel imbalance (<0.3 dB), low phase error (<0.8°) and improved cross-polar isolation (≈48 dB).

Keywords: antenna; calibration; ground penetrating radar; polarimetry

check for updates

Citation: Forster, S.J.I.; Peyton, A.J.; Podd, F.J.W. Calibration of Dual-Polarised Antennas for Air-Coupled Ground Penetrating Radar Applications. *Remote Sens.* **2024**, *16*, 4114. https://doi.org/10.3390/rs16214114

Academic Editors: Shaohui Mei, Junhui Hou, Kun Hu, Mingyang Ma

Received: 9 September 2024
Revised: 31 October 2024
Accepted: 2 November 2024
Published: 4 November 2024

Copyright: © 2024 by the authors. Licensee MDPI, Basel, Switzerland. This article is an open access article distributed under the terms and conditions of the Creative Commons Attribution (CC BY) license (https://creativecommons.org/licenses/by/4.0/).

1. Introduction

Polarimetry can be used to analyse targets by measuring the amplitude and phase information obtained from the co- and cross-polarised channels. However, in radar systems, where signals must be transmitted and received through antennas, the performance of the antennas is paramount, in particular co-polar channel balance and cross-talk in both magnitude and phase. The calibration of antennas is imperative to ensure the acquisition of accurate and reliable data; this is particularly crucial when the data are intended for further polarimetric analysis [1,2].

In past research related to the polarimetric calibration of antennas, one focus has been on Polarimetric Synthetic Aperture Radar (PolSAR) systems, particularly in the context of satellite platforms and high-altitude systems. In these studies, the calibration process typically involves the integration of calibration targets strategically placed within the PolSAR imaging scene, and the calibration parameters are derived from the analysis of the processed images [3–5].

One widely used technique in this field is the polarimetric decomposition of the PolSAR data; this relies on the accurate portrayal of amplitude and phase information as otherwise uncorrected distortions produce misleading results and misinterpreted target information. The effect of calibration on techniques such as Pauli and Yamaguchi decomposition and target scattering vector model are shown in [1,2].

Various methodologies have been developed over the years to calibrate polarimetric radar, each with their own advantages and disadvantages. Freeman et al. employed Polarimetric Active Radar Calibrators (PARCs) with adjustable polarisation signatures in the scene; however, the cross-talk calibration performance suffered with extended radar

swaths [3]. Passive radar calibrators are more commonly used; Yueh et al. derived the exact solution for three calibration targets in several different target configurations; reflectors such as dipoles, trihedrals and a general target with a cross-polar component were used. One drawback was that it was limited to the specific scattering matrices derived for [5]. Han et al. also used a dipole target and developed a calibration technique for circular quad polarisation [6]. Whitt et al., however, derived a general calibration technique with no restrictions on the form of scattering matrix used, addressing channel imbalances and cross-talk using three calibration targets [7].

Not all methods require the knowledge of the scattering matrix of the calibration targets, as shown by Nashashibi et al., who designed a coherent on-receive radar calibration technique, requiring only two calibration targets: a target with a known scattering matrix such as a sphere and a depolarising target where a known scattering matrix is not required [8].

Alternatively, Van Zyl introduced a method that uses natural targets with at least one trihedral corner reflector [4], and Feng et al. developed a comprehensive mathematical formulation that incorporated higher order terms. A dihedral target was used for the co- and cross-polar terms oriented at 0° and 45°, respectively [9]. The group applied their calibration methodology on a GPR system mounted on a moving platform [10] and later applied the calibration technique on polarimetric GPR data that were used for polarimetric migration [11].

A single calibration target may be used as Sarabandi proposed; the Isolated-Antenna Calibration Technique (IACT), however, does not account for cross-talk contamination in the antenna and can lead to significant errors [12]. An improvement to the technique achieved 50 dB cross-polar isolation [12].

A high calibration performance was achieved using the polarimetric calibration method devised by Wang et al., which utilised a trihedral, dihedral and a corner reflector, achieving an amplitude imbalance of 0.5 dB and phase error of 3° [1]. There is limited research conducted with the combination of polarimetry and Ground-Penetrating Radar (GPR), with even fewer studies incorporating polarimetric calibration procedures in their methodology. A fully polarimetric GPR system was developed by Yu et al. which calibrated the cross-talk and channel imbalance before performing Pauli decomposition. The methodology was tested on data collected from a buried metal plate, dihedral, metal bucket and chaotic scattering target [13]. Liu et al. developed a hybrid GPR system utilising circular polarisation for transmission with horizontal and vertical polarisations for receiving and was used to measure the orientation angle of buried elongated objects [14]. A time-domain calibration technique [15] was applied to their polarimetric GPR data and later improved their GPR detection technique [16]. Another technique for estimating the orientation of buried elongated objects is presented by Sun et al., who used a dual cross-polarised system, neglecting the co-polar channels for better ground rejection [17]. For this application, the manifestation of un-calibrated data would present as an error in the orientation estimate. An alternate methodology was used which used dual-polarised antennas but neglected the cross-polar component to measure the Bragg scattering of tree trunks [18]. The polarimetric decomposition techniques used in their analysis would often benefit from the calibration technique presented.

Burr et al. developed a polarimetric Unmanned Aerial Vehicle (UAV) GPR system using a 45° linear transmit antenna and horizontal and vertical receive antennas. Only the phase centre was corrected, however [19]. Wirth et al. applied a phase adjustment to correct for a bi-static angle, effectively transforming the data into an equivalent mono-static configuration; they then conducted a comparative analysis of different polarisation decomposition techniques with GPR data [2]. An overview of some of the techniques discussed in this paper are provided in Table 1. The data were collected from studies with experimentally validated and quoted calibration performance metrics, focusing on frequency domain and linear polarisation calibration techniques. The table compares the

quoted calibration performance across the measured frequency band and highlights the benefits and limitations of each technique.

Table 1. Comparison of calibration methods.

Study	Co-Polar Channel Balance (dB)	Phase Error (°)	Cx-Polar Isolation (dB)	Frequency Range (GHz)	Benefits	Limitations
Wang et al. [1]	0.5	3	-	9.5–9.6	Requires no assumptions on the scene statistics	Sensitive to orientation errors
Freeman et al. [3]	1	10.8	20–26	1.26–1.24	PARCs allow adjustable radar signatures	Performance suffers over extended radar swaths
Whitt et al. [7]	0.3	3	50	9–10	Flexibility in choosing calibration targets	Sensitive to orientation errors
Nashashibi et al. [8]	0.4	4	40	34.2–34.8	Can be calibrated with one known and one unknown object	Two-step calibration procedure
Sarabandi et al. [12]	0.3	5	25	9–10	Only requires single spherical calibration object	Does not correct for cross-polar isolation
Sarabandi et al. [20]	0.4	5	50	9–10	Corrects for cross-polar isolation	Single calibration object may be more susceptible to noise

In recent years, there has been growing interest in utilising UAVs for Ground-Penetrating Radar (GPR) applications [21]. While fully polarimetric UAV-based systems remain relatively limited, the research in this domain is expanding. This paper seeks to present a practical and straightforward method for calibrating antennas specifically designed for polarimetry, placing a particular emphasis on applications involving UAVs and GPR, where the requirements of lightweight construction and aerodynamic design may limit mechanical precision and hence the resulting Electromagnetic (EM) performance of the antennas. As mentioned in this review, many calibration techniques have been developed, predominately focused on air-borne systems with in-scene reflectors. The limitations of these methods are the lack of flexibility of the calibration target placement, which is understandable for airborne systems that inherently lack this option; however, applications of UAV-based GPR systems allow greater flexibility in the target chosen, its placement and orientation. Some methodologies lack targets with a cross-polar component, which is required to calibrate all polarisation components. The techniques mentioned use up to three calibration targets in order to gain the polarisation diversity; however, with only three measurements, the method may be more susceptible to noise and errors. The proposed methodology addresses these limitations by using a system to capture more information of the calibration target, rejecting noise and creating a more stable solution. Using a thin metallic cylinder placed on a rotating system, the scattering matrices of the cylinder are measured around 360° in 200 rotational positions; this produces 100 distinct scattering matrices and

two measurements for each orientation, allowing the formation of an over-determined inverse problem which can be solved in a robust and effective manner. The proposed method does, however, require knowledge of the scattering matrix, which, for a simple elongated target, is trivial. Despite this, the methodology offers a straightforward, robust and cost-effective solution which has greater flexibility for UAV and GPR-based systems, as it is specifically designed for this application. For UAV-based systems, a lightweight antenna design is critical; these designs often lack the mechanical rigidity and precision offered by antennas made from thicker metal, and this then requires the calibration of the antenna post-manufacture to correct for the misalignment and performance issues. To illustrate this, this study presented a second antenna with poor performance, which was corrected using the proposed method. Highlighting the versatility of this method, by enabling the correction of antennas with manufacturing defects allows greater choice in antenna design to align with the lightweight and aerodynamic requirements of UAV systems.

2. Methodology

2.1. Calibration Model

The following presents part of the authors contribution; this section outlines the theoretical foundation for the calibration procedure. For un-calibrated antennas, the measurement of a scattering matrix is distorted by the antennas characteristics; this distortion includes an imbalance in co-polar return amplitudes, a phase mismatch between co-polar components and a low level of cross-polar isolation [1–5]. For instance, a polarimetric measurement of a large plate should provide an equal return amplitude and phase for both co-polar HH and VV components. An antenna may have different characteristics of its co-polar channels, leading to differences in the measured amplitude and phase of the HH and VV components, equating to misinterpreted target information. The aim of the antenna calibration is to correct for these antenna distortions such that the target polarisation properties are accurately measured. In this study, the error between the measured scattering matrix and the known scattering matrix of the calibration object is captured. In order to correct for these errors, a model of the system was developed to map the known scattering matrix, S_c, to the measured scattering matrix, M, using a calibration matrix, A_c, and a calibration offset matrix, C.

The scattering matrix M represents the measured response from the target, incorporating both the target response and any distortions introduced by the antenna. In contrast, the matrix S_c denotes the ideally measured scattering matrix of the target, without the influence of the antenna. The calibration matrix, A_c, is designed to adjust the measured scattering matrix, M, to account for systematic errors, representing the linear transformation necessary for correcting the measurements. Meanwhile the offset matrix, C, captures any constant or offsets in the measurements, accounting for additional errors that may not be linearly related to the measured values. The system model that was chosen to represent this transformation is given by

$$S_c = A_c M + C \tag{1}$$

where all quantities are complex frequency-dependent 2×2 matrices, which take the form

$$\begin{bmatrix} S_{c00} & S_{c01} \\ S_{c10} & S_{c11} \end{bmatrix} = \begin{bmatrix} A_{c00} & A_{c01} \\ A_{c10} & A_{c11} \end{bmatrix} \cdot \begin{bmatrix} M_{00} & M_{01} \\ M_{10} & M_{11} \end{bmatrix} + \begin{bmatrix} C_{00} & C_{01} \\ C_{10} & C_{11} \end{bmatrix} \tag{2}$$

A thin elongated metallic cylinder, later discussed in Section 2.3, was used as the calibration object. The scattering matrix of this target is analogous to the Jones Matrix for a linear polariser. When aligned with the horizontal axis, this matrix is given by [22,23]

$$S = \begin{bmatrix} 1 & 0 \\ 0 & 0 \end{bmatrix} \tag{3}$$

The measurement of this scattering matrix in isolation lacks the polarisation diversity required to fully calibrate the system. More measurements with diverse scattering matrices

are needed; to answer this requirement, the thin elongated metallic cylinder was rotated around the antenna bore-sight whilst obtaining measurements at discrete rotation angles described by θ. This, in the theoretical sense, may be represented by rotating a polarising element, such as the linear polariser, to the equivalent orientations provided by the physical alignment of the metallic cylinder. Thus, for a rotating polarising element, the Jones matrix is expressed as [22,23]

$$S_c(\theta) = J_{ROT}(-\theta) \cdot S_c \cdot J_{ROT}(\theta) \tag{4}$$

In this expression, θ represents the angular position of the calibration object and, equivalently, the rotation angle of the theoretical linear polariser. $J_{ROT}(\theta)$ represents the rotation matrix, $J_{ROT}(-\theta)$ is the inverse rotation matrix and $S_c(\theta)$ denotes the rotated scattering matrix. Including the scattering matrix of the calibration target (S_c) in Equation (4) results in the following representation of the rotating metallic cylinder. This equation is widely used in optics and electromagnetism [14,17,23].

$$S_c(\theta) = \begin{bmatrix} \cos(\theta) & -\sin(\theta) \\ \sin(\theta) & \cos(\theta) \end{bmatrix} \cdot \begin{bmatrix} 1 & 0 \\ 0 & 0 \end{bmatrix} \cdot \begin{bmatrix} \cos(\theta) & \sin(\theta) \\ -\sin(\theta) & \cos(\theta) \end{bmatrix} \tag{5}$$

To determine the unknown quantities A_c and C, an inverse problem methodology was employed. First, Equation (2) is rewritten into a system of simultaneous linear equations.

$$\begin{aligned} S_{c00} &= A_{c00}M_{00} + A_{c01}M_{10} + C_{00} \\ S_{c01} &= A_{c00}M_{01} + A_{c01}M_{11} + C_{01} \\ S_{c10} &= A_{c10}M_{00} + A_{c11}M_{10} + C_{10} \\ S_{c11} &= A_{c10}M_{01} + A_{c11}M_{11} + C_{11} \end{aligned} \tag{6}$$

The calibration process involves a phase correction, aligning the calibrated phase to the location of the calibration target. As this is placed at an arbitrary distance, a phase offset is applied to ensure the measured delay is consistent with subsequent measurements, giving the true delay to the target. Thus, the phase of the scattering matrix, S_c, is adjusted to align with the measurement matrix, M, using a phase factor [23–25]

$$e^{-i\omega r/V_m} \tag{7}$$

where ω is the angular frequency, r is the range to the calibration target and V_m is the velocity of the electromagnetic wave in the medium.

Rewriting the linear equations from Equation (6) into a linear system of equations in the form $y = Bx$ yields the bi-static matrix equation for a single rotation angle and a single frequency point, donated by the index i

$$\begin{bmatrix} S_{c00i} \\ S_{c01i} \\ S_{c10i} \\ S_{c11i} \end{bmatrix} e^{-i\omega r/V_m} = \begin{bmatrix} M_{00i} & M_{10i} & 0 & 0 & 1 & 0 & 0 & 0 \\ M_{01i} & M_{11i} & 0 & 0 & 0 & 1 & 0 & 0 \\ 0 & 0 & M_{00i} & M_{10i} & 0 & 0 & 1 & 0 \\ 0 & 0 & M_{01i} & M_{11i} & 0 & 0 & 0 & 1 \end{bmatrix} \begin{bmatrix} A_{c00} \\ A_{c01} \\ A_{c10} \\ A_{c11} \\ C_{00} \\ C_{01} \\ C_{10} \\ C_{11} \end{bmatrix} \tag{8}$$

For a mono-static system where $S_{c01} = S_{c10}$, the equivalent equation is expressed in Equation (9)

$$\begin{bmatrix} S_{c00i} \\ S_{c01i} \\ S_{c11i} \end{bmatrix} e^{-i\omega r/V_m} = \begin{bmatrix} M_{00i} & M_{10i} & 0 & 0 & 1 & 0 & 0 & 0 \\ \frac{M_{01i}}{2} & \frac{M_{11i}}{2} & \frac{M_{00i}}{2} & \frac{M_{10i}}{2} & 0 & 0.5 & 0.5 & 0 \\ 0 & 0 & M_{01i} & M_{11i} & 0 & 0 & 0 & 1 \end{bmatrix} \begin{bmatrix} A_{c00} \\ A_{c01} \\ A_{c10} \\ A_{c11} \\ C_{00} \\ C_{01} \\ C_{10} \\ C_{11} \end{bmatrix} \tag{9}$$

To find a solution for A_c and C that satisfies all rotation angles, the system of equations is expanded to include N rotation angles. As a result, the rows of B and y increase by $4N$ and $3N$ for bi-static and mono-static, respectively. A regularised least squares approach was employed to solve x for each frequency point, which results in frequency-dependent calibration factors A_c and C. This equation is shown in Equation (10) [26].

$$x = (B^H \cdot B + \lambda I)^{-1} \cdot B^H y \tag{10}$$

Here, B^H denotes the conjugate transpose of matrix B, and a Tikhonov regularisation parameter, λ, was introduced to enhance the robustness of the inversion process, where the regularisation parameter, λ, is a non-negative value and I is the identity matrix of B.

2.2. Polarisation Decomposition

To illustrate the efficacy of the calibration, Pauli decomposition, a widely used polarimetric analysis technique was utilised to create colour composite images of different scattering phenomena. This technique separates scattering mechanisms into single, double and volume-scattering behaviours based on the corresponding scattering matrices [27,28].

$$p_1 = \frac{1}{\sqrt{2}} \begin{bmatrix} 1 & 0 \\ 0 & 1 \end{bmatrix}, \quad p_2 = \frac{1}{\sqrt{2}} \begin{bmatrix} 1 & 0 \\ 0 & -1 \end{bmatrix}, \quad p_3 = \frac{1}{\sqrt{2}} \begin{bmatrix} 0 & 1 \\ 1 & 0 \end{bmatrix} \tag{11}$$

These scattering matrices yield the equivalent Pauli coefficients,

$$s_1 = \frac{1}{\sqrt{2}}(HH + VV), \quad s_2 = \frac{1}{\sqrt{2}}(HH - VV), \quad s_3 = \frac{2}{\sqrt{2}}(HV) \tag{12}$$

In the case of a mono-static system where reciprocity holds and $HV = VH$, then s_3 is twice one of the cross-polar components.

2.3. Calibration Measurement Setup

The experimental setup depicted in Figure 1 employed a modified 3 m long camera boom, a Copper Mountain Technologies Vector Network Analyser (VNA), a rotation system and two quad-ridged antennas. According to the manufacturer's specifications, these antennas provide a cross-polarisation isolation of less than 35 dB and a gain that increases from 6 to 12 dBi across the operating range of 1 to 6.5 GHz.

The rotation system was designed for precise angular measurements of a thin elongated metallic cylinder, used as a calibration object. This cylinder had a length of 0.3 m and a diameter of 5 mm. The rotation system utilised a stepper motor, motor driver electronics and an Arduino for facilitating communications between the PC and controlling the motor driver. The stepper motor spindle extended through an 11.5 cm thick piece of Radar Absorbent Material (RAM), which minimised spurious signals. A diagram of the setup is shown in Figure 2.



Figure 1. Experimental setup of the calibration measurement system.

Measurements for each antenna were obtained by mounting the quad-ridged antennas separately onto the modified camera boom. These antennas were positioned in a downward looking geometry aligned with the z-axis, maintaining a vertical distance of 0.5 m between the antenna tip and the cylinder. The antenna bore-sight was aligned with the cylinder's centre axis of rotation to ensure that accurate measurements of the cylinders scattering matrix were obtained. The cylinder was incrementally rotated in the xy-plane through 360° in 200 steps, corresponding to a step size of 1.8°. Using the VNA configured with the settings outlined in Table 2, polarimetric measurements of the calibration object were obtained at each angle. The experimental setup is illustrated in Figure 1.

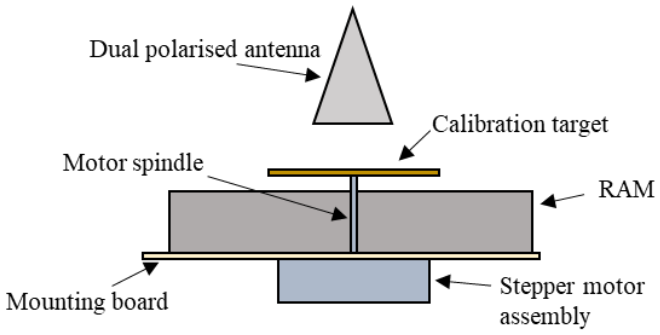


Figure 2. Rotation system diagram.

Table 2. VNA Settings.

Start Frequency (GHz)	Stop Frequency (GHz)	Intermediate Frequency (kHz)	Frequency Points
1	6.5	10	202

2.4. GPR Measurement Setup

To acquire polarimetric GPR measurements of a buried target, the same two antennas detailed in Section 2.3 were used to obtain two B-Scans, one for each antenna. The experi-

mental setup, as seen in Figure 3, included a perspex tank filled with sand, which measured 1.0 × 1.0 × 0.4 m, and a 3-axis positioning system. The target chosen was a CD which measured 12 cm in diameter and was buried at a depth of 15 cm. The antennas were placed 0.4 m above the surface of the sand in a downward looking configuration and were moved across 0.94 m in 100 steps. A Keysight VNA was used to acquire these measurements with the same settings outlined in Table 2.



Figure 3. Experimental setup of the B-Scan acquisition with Antenna-1, Antenna-2, 3-axis positioning system and sandpit.

3. Results

The following results section explains the calibration measurements and the verification of the calibration performance when applied to measurements of the cylinder target and a GPR B-Scan of a buried object. Two antennas of differing performance were used to illustrate the application of this technique; the two antennas were denoted as Antenna-1 and Antenna-2, which correspond to the good and poor performing antennas, respectively.

3.1. Calibration

3.1.1. Pre-Processing

To minimise the effects of noise and clutter, a background measurement was acquired and removed from subsequent calibration measurements. An Inverse Fast Fourier Transform (IFFT) with a Tukey window ($\alpha = 0.1$) was applied to transition to the time-domain in order to isolate the reflection from the calibration target; this further removed background noise. The Tukey window was chosen to minimise the filtering of the high and low frequency components. Subsequently, a Fast Fourier Transform (FFT) was used to transition back to the frequency domain.

3.1.2. Calibration Measurements and Performance

Using the setup explained in Section 2.3, full rotational polarimetric measurements of the cylinder were obtained. These were repeated to facilitate the calculation of the calibration parameters and verification of the calibration performance. Using 200 rotational positions, the solution of the frequency-dependent calibration parameters were determined using Equation (9). The effectiveness of the calibration process is evident in the comparison between the ideal scattering matrix in Figure 4, the pre- and post-calibration results in Figure 5 and the frequency band performance in Figure 6. Each rotation angle of the cylinder presents a different scattering matrix; Figure 5 shows the mid-band (3.75 GHz) measured scattering matrices over rotation angle, and as such, the calibration performance of the system for measuring various scattering matrices. For object orientation estimation, this methodology could prove useful as it ensures that the measurement of the objects orientation angle corresponds to its true orientation. Measuring the object with rotation offers

a new dimension in the performance analysis, which describes not only one measurement of a calibration target but also gives the performance of the system as it relates to many scattering matrices.

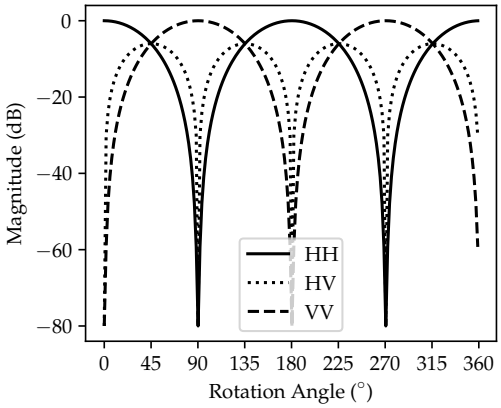


Figure 4. Magnitude of the ideal scattering matrix versus rotation angle.

Analysing the figures allows for a comparison of the co-polar channel balance and cross-polar isolation before and after calibration for each antenna. The channel balance can be seen by the difference in magnitude between HH and VV components, observed at angles where the calibration object aligns with each of the co-polar axes. For instance, HH is aligned at 0°, 180° and 360°, whilst VV is aligned at 90° and 270°. Upon comparing the pre-calibration performance depicted in Figure 5a,c, it is evident that Antenna-2 exhibits significantly poorer channel balance compared to Antenna-1, which initially demonstrated well-balanced performance. Meanwhile, the cross-polar isolation can be observed in the difference in magnitudes between the co- and cross-polar components at the equivalent angles for HH and VV components. Comparing to Figure 5b,d where both antennas following calibration, demonstrates well balanced co-polar components, lower cross-polar minimums and an improved curve shape.

At 45°, 135°, 225° and 315°, all polarisation components should ideally be equal and the scattering matrix should have a magnitude of 0.5 in each element. At these angles, both antennas exhibit higher magnitude cross-polar components, which are then significantly improved in Figure 5b,d.

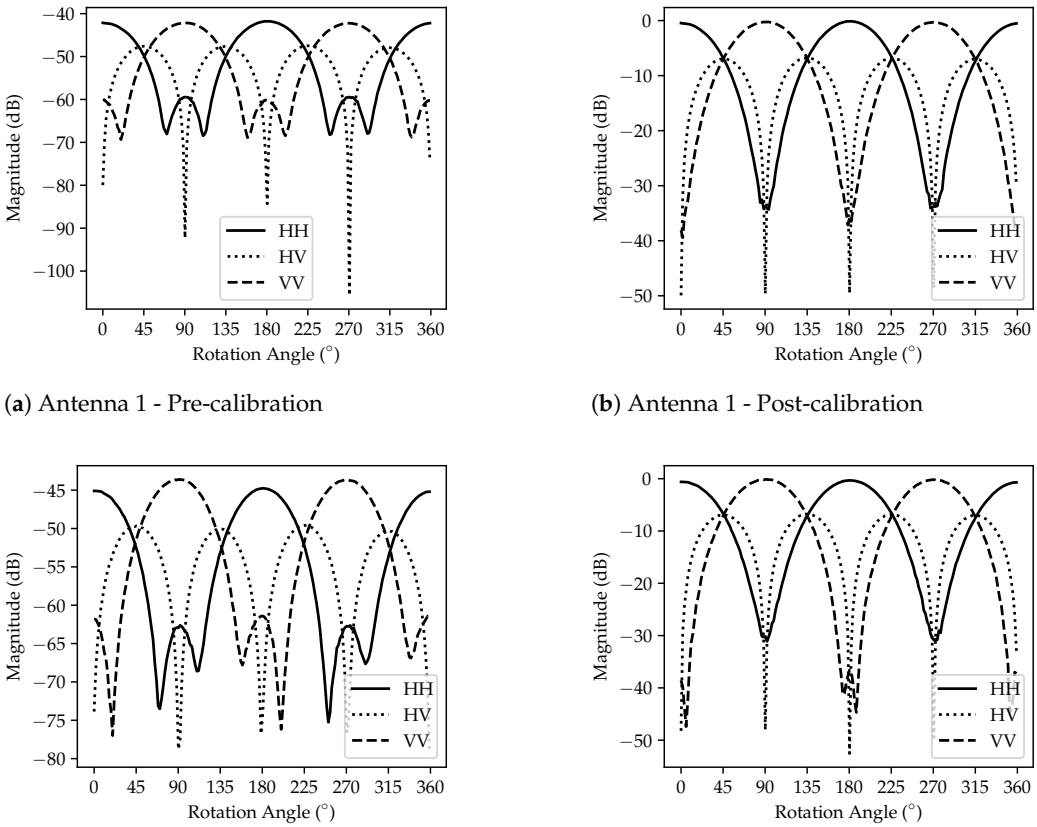
For a detailed overview of the calibration performance regarding these parameters, refer to Tables 3 and 4, which show the average mid-band performance over a full rotation.

Table 3. Pre-calibration performance.

Antenna	Channel Balance (dB)	Phase Error (°)	Cx-Polar Isolation 1 (dB)	Cx-Polar Isolation 2 (dB)
1	0.23	5.37	40.16	56.76
2	1.30	3.58	29.21	34.02

Table 4. Post-calibration performance.

Antenna	Channel Balance (dB)	Phase Error (°)	Cx-Polar Isolation 1 (dB)	Cx-Polar Isolation 2 (dB)
1	0.02	0.32	49.42	48.85
2	0.29	0.79	49.92	48.61



(**a**) Antenna 1 - Pre-calibration

(**b**) Antenna 1 - Post-calibration

(**c**) Antenna 2 - Pre-calibration

(**d**) Antenna 2 - Post-calibration

Figure 5. Magnitude versus rotation angle performance of Antenna-1 and Antenna-2 pre- and post-calibration.

A notable improvement is observed in the cross-polar isolation for Antenna-2, which has been significantly enhanced by approximately 20 dB. For post-calibration, as shown in Table 4, both antennas demonstrate similar performance across all parameters.

In polarimetry, it is often useful to analyse the target scattering matrix to ensure that these measurements align with the calibrated theoretical scattering matrix of a linear polariser. The scattering matrix of the cylinder was measured in two positions: one aligned with the H axis and the other with the V axis. The results of these measurements were examined both before and after calibration and are presented in Tables 5 and 6.

Table 5. Pre-calibration scattering matrix.

Antenna	HH	HV	VV
1	7.97×10^{-3}	8.05×10^{-5}	7.76×10^{-3}
2	5.67×10^{-3}	1.95×10^{-4}	6.58×10^{-3}

Table 6. Post-calibration scattering matrix.

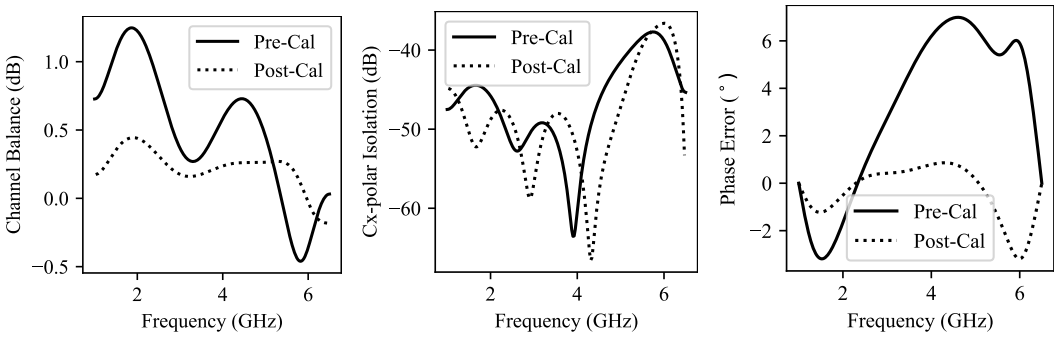
Antenna	HH	HV	VV
1	0.97	2.69×10^{-3}	0.97
2	0.95	1.48×10^{-3}	0.98

After the calibration process, both antennas demonstrate excellent agreement in their measurement of the scattering matrices, closely matching the theoretical values.

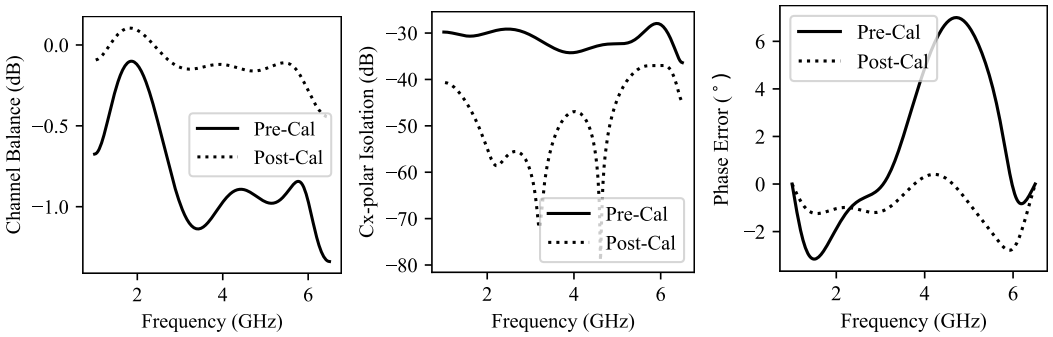
The following plots in Figure 6 show the calibration performance variation over frequency, for channel balance, cross-polar isolation and phase error for both Antenna-1 and Antenna-2 for pre- and post-calibration results.

The channel balance for Antenna-1, as shown in Figure 6a, has improved from 1.5 dB pre-calibration to 0.5 dB post-calibration across the entire frequency range. The variation with frequency has also been considerably reduced, allowing for the accurate portrayal of co-polar target returns across the frequency range. The cross-polar isolation has remained largely equivalent post-calibration, indicating the antenna's good initial performance in this metric. The post-calibration phase error, however, shows a much lower figure across the band, reducing from 6.5° to 2° for pre- and post-calibration results, respectively. Minimising the variation with frequency ensures the accurate phase of the target is recovered; this will aid in subsequent polarimetric analysis and for SAR applications where the phase delay is vitally important for accurate target localisation.

In contrast, the results for Antenna-2 have improved more considerably across all metrics. Pre-calibration, the antenna exhibited worse performance in the channel balance, significantly worse performance in the cross-polar isolation and similar performance in phase balance when considering across-the-band results.



(**a**) Antenna-1 channel balance (**b**) Antenna-1 cx-polar isolation (**c**) Antenna-1 phase error



(**d**) Antenna-2 channel balance (**e**) Antenna-2 cx-polar isolation (**f**) Antenna-2 phase error

Figure 6. Pre- and post-calibration results of channel balance, cross-polar isolation and phase error across the frequency band (1–6.5 GHz).

Specifically, the channel balance reduced from 1.4 dB to within 0.5 dB, comparable now to Antenna-2 post-calibration. The cross-polar isolation is the worst performing metric for Antenna-2 and is likely the main contributing factor for its poor performance. Post-calibration, however, cross-polar isolation has improved from −30 dB to a comparable level and response to Antenna-1 of approximately −50 dB. The phase error follows a similar frequency variation to Antenna-1, which has been significantly reduced to within 2° across the band from over 6° error. The proposed methodology offers a potential performance improvement over the techniques provided in Table 1 for this context, which has been validated over an ultra-wide frequency band within the near-field of the antenna.

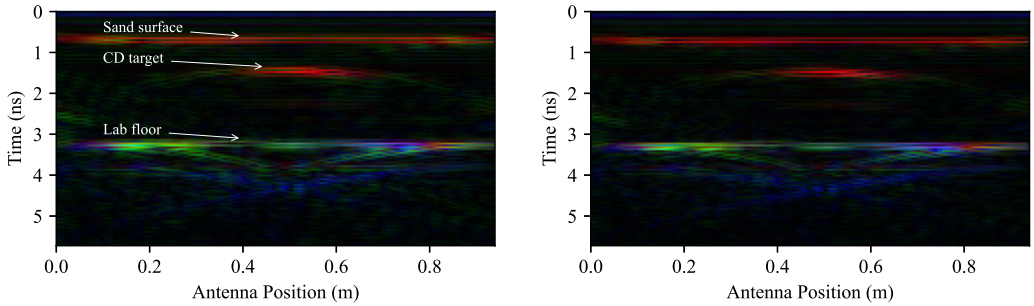
This highlights the suitability of this technique for close-range, air-coupled polarimetric GPR measurements.

3.2. Verification on Ground Penetrating Radar Data

The calibration parameters generated from the initial cylinder measurements are applied to radar data acquired using the Keysight VNA, as detailed in Section 2.4. The data are presented in the form of a B-Scan, acquired using the same dual-polarised antennas. The experimental setup is shown in Figure 3.

Pauli decomposition, a technique detailed in Equation (12), was employed to showcase the calibration performance. This method organises reflections into three scattering mechanisms—single bounce, double bounce and volume scattering—which are then applied to a 3-channel image as red, green and blue to represent each mechanism, respectively. The resulting images in Figure 7a–d reveal distinct features, as highlighted in Figure 7a.

For instance, a horizontal band at 0.7 ns represents the reflection from the sand surface, while the CD reflection is observed at 1.5 ns in the centre of the image. At 3.2 ns, reflections from the lab floor are visible.



(**a**) Antenna 1 - Pre-calibration B-Scan

(**b**) Antenna 1 - Post-calibration B-Scan

(**c**) Antenna 2 - Pre-calibration B-Scan

(**d**) Antenna 2 - Post-calibration B-Scan

Figure 7. Calibration performance of GPR data displayed using colour composite images of Pauli decomposition. Each colour channel (RGB) represents $R = \frac{1}{\sqrt{2}}(HH + VV)$, $G = \frac{1}{\sqrt{2}}(HH - VV)$ and $B = \frac{2}{\sqrt{2}}(HV)$.

It should be noted that each of the Pauli coefficients was normalised separately. This means that the relative amplitudes of each colour channel in the resulting images are not representative of the returned reflection power. For example, the single bounce (red channel) would represent a much stronger reflection compared to the other scattering mechanisms. If a group normalisation approach had been used, the prominence of the single bounce reflection would overshadow the other features, making them less visible and the effect of calibration less noticeable.

The differing performance of Antenna-1 in Figure 7a and Antenna-2 in Figure 7c is evident when comparing the scattering characteristics of the sand surface and CD. Although both targets exhibit strong single bounce reflections, the scattering image produced

by Antenna-2 lacks clarity in representing the single bounce component (red). In the case of single bounce targets, balanced co-polar channels should cancel out the second Pauli coefficient (green); therefore, the residual imbalances are seen in green. The performance of Antenna-2 is substantially improved in Figure 7d post-calibration, showing a significant improvement in channel balance.

Similarly, despite Antenna-1 initially producing satisfactory images, the calibration has had a marked improvement in the co-polar balancing, leading to better cancellation of the second Pauli coefficient when comparing Figure 7a,b.

There is a noticeable phase offset between the co-polar channels in Figure 7c, causing misalignment of the time-domain impulses. This contributes to the inaccurate measurement of the targets scattering behaviour, leading to misinterpreted target identification. The improvement in the phase error is evident when examining Figure 7c,d.

In addition to this verification, two further studies were conducted using this calibration methodology, which proved to be an essential and valuable component in both cases. The first study, which was presented at SPIE Sensors and Imaging 2024 under the title 'Polarimetric 3D SAR Imaging and Analysis of Polarization Signatures for Enhanced Subsurface Detection', included the calibration and measurement of a buried metallic sphere with a 5 cm diameter. Analysis of its polarisation signature before and after calibration demonstrated a significant improvement, aligning closely with the theoretical expectations of the polarisation signature for a spherical target showing minimal orientation dependence and cross-polar return power. The second study, titled 'Polarisation Synthesis Applied to 3D Polarimetric Imaging for Enhanced Buried Object Detection and Identification,' submitted to MDPI's *Remote Sensing*, *Image Processing*, also implemented this calibration. This study applied the principle of polarisation synthesis to the measurements of various buried objects, including shallowly buried wires and an empty plastic container, to create new polarisation states. Polarisation synthesis requires precise polarimetric data to reliably produce the intended polarisation. As such, the calibration played a critical role in correcting antenna distortions, without which the synthesised polarisations would not align with theoretical models and would appear offset from the intended polarisation. Following calibration, linear polarisations at multiple orientation angles, as well as left- and right-hand circular polarisations, were accurately synthesised, further validating the proposed calibration methodology.

4. Conclusions

This study offers a cost-effective method for calibrating dual-polarised antennas for GPR applications. Standard calibration targets can range from USD 300 to USD 10,000; the proposed methodology cost <USD 100. Unlike other methodologies which use three to four independent scattering matrices sensitive to manual alignment, the proposed method derives the calibration parameters from 100 distinct scattering matrices using a precise angular system, reducing noise and outliers for an accurate and stable solution. The calibration procedure was successfully applied to a faulty antenna with significant manufacturing defects, resulting in greatly improved phase, amplitude balance and cross-polar isolation across the full frequency band, achieving the performance level of a fully functional antenna. This method is particularly useful for UAV-based systems, where the requirements of lightweight and aerodynamic antennas can severely limit the mechanical rigidity and manufacturing precision. The calibration procedure was additionally validated on a real-world scenario of GPR data collected in a lift-off scenario similar to low flying UAVs; both antennas showed comparable performance post-calibration. The methodology applied in the near-field of the antenna not only advances the practicality of antenna calibration in GPR applications where close-range calibration is often required but also underscores the importance of cost-effective solutions in advancing radar technology.

5. Future Work

The current calibration methodology corrects for the antenna polarisation parameters on bore-sight. Extending this method to account for off bore-sight polarisation variations could enhance accuracy in more complex 3D measurement scenarios. Furthermore, it is evident that ground properties can distort the polarisation response of a target. Thus, an additional calibration process that incorporates the electromagnetic characteristics of the ground at the test location could improve the accuracy of polarimetric measurements for buried targets.

Author Contributions: Conceptualization, S.J.I.F., A.J.P. and F.J.W.P.; data curation, S.J.I.F.; formal analysis, S.J.I.F., A.J.P. and F.J.W.P.; funding acquisition, A.J.P. and F.J.W.P.; investigation, S.J.I.F.; methodology, S.J.I.F., A.J.P. and F.J.W.P.; project administration, A.J.P. and F.J.W.P.; resources, A.J.P. and F.J.W.P.; software, S.J.I.F.; supervision, A.J.P. and F.J.W.P.; validation, S.J.I.F., A.J.P. and F.J.W.P.; visualization, S.J.I.F.; writing—original draft, S.J.I.F.; writing—review and editing, S.J.I.F., A.J.P. and F.J.W.P. All authors have read and agreed to the published version of the manuscript.

Funding: This research is funded by the Engineering and Physical Sciences Research Council (EPSRC) and the Defence Science and Technology Laboratory (Dstl), under iCASE voucher 19000062.

Data Availability Statement: The data supporting this study are available from the corresponding author upon reasonable request. Access to the data may be granted after obtaining the necessary permissions.

Conflicts of Interest: The authors declare no conflicts of interest.

References

1. Wang, S.; Chen, K.S.; Sato, M. Performance of SAR polarimetric calibration using hybrid corner reflectors: Numerical simulations and experimental measurements. *IEEE J. Sel. Top. Appl. Earth Obs. Remote Sens.* **2021**, *14*, 440–451. [CrossRef]
2. Wirth, S.; Morrow, I. Comparison of polarimetric decomposition techniques to suppress subsurface clutter in GPR applications. In Proceedings of the Loughborough Antennas Propagation Conference 2018, Loughborough, UK, 12–13 November 2018; p. 53. [CrossRef]
3. Freeman, A.; Shen, Y.; Werner, C. Polarimetric SAR calibration experiment using active radar calibrators. *IEEE Trans. Geosci. Remote Sens.* **1990**, *28*, 224–240. [CrossRef]
4. van Zyl, J. Calibration of polarimetric radar images using only image parameters and trihedral corner reflector responses. *IEEE Trans. Geosc. Remote Sens.* **1990**, *28*, 337–348. [CrossRef]
5. Yueh, S.H.; Kong, J.A.; Barnes, R.B.; Shin, R.T. Calibration of polarimetric radars using in-scene reflectors. *J. Electromagn. Waves Appl.* **1990**, *4*, 27–48. [.]. [CrossRef]
6. Han, Y.; Lu, P.; Liu, X.; Hou, W.; Gao, Y.; Yu, W.; Wang, R. On the method of circular polarimetric SAR calibration using distributed targets. *IEEE Trans. Geosci. Remote Sens.* **2023**, *61*, 5203216. [CrossRef]
7. Whitt, M.; Ulaby, F.; Polatin, P.; Liepa, V. A general polarimetric radar calibration technique. *IEEE Trans. Antennas Propag.* **1991**, *39*, 62–67. [CrossRef]
8. Nashashibi, A.; Sarabandi, K.; Ulaby, F. A calibration technique for polarimetric coherent-on-receive radar systems. *IEEE Trans. Antennas Propag.* **1995**, *43*, 396–404. [CrossRef]
9. Feng, X.; Zou, L.; Lu, Q.; Liu, C.; Liang, W.; Zhou, Z.S. Calibration with high-order terms of polarimetric GPR. *IEEE J. Sel. Top. Appl. Earth Obs. Remote Sens.* **2012**, *5*, 717–722. [CrossRef]
10. Feng, X.; Wang, Q.; Lu, Q.; Liu, C.; Liang, W.; Li, H.; Ren, Q.; Yu, Y.; Shu, Z. Developing moving platform mounted polarimetric GPR system. In Proceedings of the 2012 14th International Conference on Ground Penetrating Radar (GPR), Shanghai, China, 2012, 4–8 June 2012; pp. 53–56. [CrossRef]
11. Feng, X.; Yu, Y.; Liu, C.; Fehler, M. Subsurface polarimetric migration imaging for full polarimetric ground-penetrating radar. *Geophys. J. Int.* **2015**, *202*, 1324–1338. [CrossRef]
12. Sarabandi, K.; Ulaby, F.; Tassoudji, M. Calibration of polarimetric radar systems with good polarization isolation. *IEEE Trans. Geosci. Remote Sens.* **1990**, *28*, 70–75. [CrossRef]
13. Yu, Y.; Feng, X.; Liu, C.; Lu, Q.; Hu, N.; Ren, Q.; Nilot, E.; You, Z.; Liang, W.; Fang, Y. Radar polarimetry analysis applied to fully polarimetric Ground Penetrating Radar. In Proceedings of the 15th International Conference on Ground Penetrating Radar, Brussels, Belgium, 30 June–4 July 2014; pp. 642–646. [CrossRef]
14. Liu, H.; Huang, X.; Han, F.; Cui, J.; Spencer, B.F.; Xie, X. Hybrid polarimetric GPR calibration and elongated object orientation estimation. *IEEE J. Sel. Top. Appl. Earth Obs. Remote Sens.* **2019**, *12*, 2080–2087. [CrossRef]
15. Pancera, E.; Zwick, T.; Wiesbeck, W. Full polarimetric time domain calibration for UWB Radar systems. In Proceedings of the 2009 European Radar Conference, Rome, Italy, 30 September–2 October 2009; pp. 105–108.

16. Liu, H.; Ding, F.; Li, J.; Meng, X.; Liu, C.; Fang, H. Improved detection of buried elongated targets by dual-polarization GPR. *IEEE Geosci. Remote Sens. Lett.* **2023**, *20*, 1–5. [CrossRef]
17. Sun, H.H.; Lee, Y.H.; Luo, W.; Ow, L.F.; Yusof, M.L.M.; Yucel, A.C. Dual-cross-polarized GPR measurement method for detection and orientation estimation of shallowly buried elongated object. *IEEE Trans. Instrum. Meas.* **2021**, *70*, 1–12. [CrossRef]
18. Zou, L.; Tosti, F.; Alani, A.M. Nondestructive inspection of tree trunks using a dual-polarized ground-penetrating radar system. *IEEE Trans. Geosci. Remote. Sens.* **2022**, *60*, 5917108. [CrossRef]
19. Burr, R.; Schartel, M.; Mayer, W.; Walter, T.; Waldschmidt, C. Uav-based polarimetric synthetic aperture radar for mine detection. In Proceedings of the 2019 IEEE International Geoscience and Remote Sensing Symposium, Yokohama, Japan, 28 July–2 August 2019; pp. 9208–9211. [CrossRef]
20. Sarabandi, K.; Ulaby, F. A convenient technique for polarimetric calibration of single-antenna radar systems. *IEEE Trans. Geosci. Remote Sens.* **1990**, *28*, 1022–1033. [CrossRef]
21. López, Y.A.; García-Fernández, M.; Álvarez-Narciandi, G.; Las-Heras, F. Unmanned aerial vehicle-based ground-penetrating radar systems: A review. *IEEE Geosci. Remote Sens. Mag.* **2022**, *10*, 66–86. [CrossRef]
22. Collet, E. *Field Guide to Polarisation*; SPIE: Bellingham, WA, USA, 2005; pp. 59–60.
23. Jones, R.C. A new calculus for the treatment of optical systems I. Description and discussion of the calculus. *J. Opt. Soc. Am.* **1941**, *31*, 488–493. [CrossRef]
24. Oppenheim, A.V.; Willsky, A.S.; Nawab, S.H. *Signals and Systems*, 2nd ed.; Prentice Hall: Upper Saddle River, NJ, USA, 1996.
25. Maxwell, J.C. A dynamical theory of the electromagnetic field. *Philos. Trans. R. Soc. Lond.* **1865**, *155*, 459–512.
26. Tikhonov, A.N. Regularization of incorrectly posed problems. *Sov. Math. Dokl.* **1963**, *4*, 1035–1038.
27. Irena Hajnsek, Y. *Polarimetric Synthetic Aperture Radar: Principles and Application*; Springer Nature: Cham, Switzerland, 2021. [CrossRef]
28. Chen, S.W.; Xuesong, W.; Xiao, S.P.; Sato, M. *Target Scattering Mechanism in Polarimetric Synthetic Aperture Radar—Interpretation and Application*; Springer: Singapore, 2018. [CrossRef]

Disclaimer/Publisher's Note: The statements, opinions and data contained in all publications are solely those of the individual author(s) and contributor(s) and not of MDPI and/or the editor(s). MDPI and/or the editor(s) disclaim responsibility for any injury to people or property resulting from any ideas, methods, instructions or products referred to in the content.